Climate responses and their hemispheric differences under an extreme quiet sun scenario

Han-Li Liu[1], Matthias Rempel[1], Gokhan Danabasoglu[2], Stanley C. Solomon[1] and Joseph M. McInerney[1]

[1]High Altitude Observatory, National Center for Atmospheric Research, Boulder, Colorado, USA
[2]Climate and Global Dynamics, National Center for Atmospheric Research, Boulder, Colorado, USA

Key Points:

- Climate simulations under extreme quiet sun conditions reveal robust responses.
- Hemispheric differences in the interplay between dynamical and radiative processes identified.
- Quantify tropospheric/surface and stratospheric responses that are similar or different.

Corresponding author: H.-L. Liu, `liuh@ucar.edu`

Abstract

Fundamental understanding of the climate responses to solar variability is obscured by the large and complex climate variability. This long-standing issue is addressed here by examining climate responses under an extreme quiet sun (EQS) scenario, obtained by making the sun void of all magnetic fields. It is used to drive a coupled climate model with whole atmosphere and ocean components. The simulations reveal robust responses, and elucidate aspects of the responses to changes of troposphere/surface forcing and stratospheric forcing that are similar and those that are different. Planetary waves (PWs) play a key role in both regional climate and the mean circulation changes. Intermediate scale stationary waves and regional climate respond to solar forcing changes in the troposphere and stratosphere in a similar way, due to similar subtropical wind changes in the upper troposphere. The patterns of these changes are similar to those found in a warming climate, but with opposite signs. Responses of the largest scale PW during NH and SH winters differ, leading to hemispheric differences in the interplay between dynamical and radiative processes. The analysis exposes remarkable general similarities between climate responses in EQS simulations and those under nominal solar minimum conditions, even though the latter may not always appear to be statistically significant.

Plain Language Summary

Understanding how climate may change under different solar conditions is both interesting and important. However it is difficult to clearly identify solar signal from the very large climate variability on broad time scales. In this study, we tackle this problem by providing a lower bound of the solar minimum condition according to our current understanding of solar physics. By specifying this extremely low solar minimum condition in a climate model that takes into consideration of the effects of ocean and middle atmosphere, we are able to identify robust climate responses, which are very different between the northern and southern hemispheres. We gain an understanding of the processes driving these responses, including how the lower and upper atmospheric processes may enhance/offset each other. By comparing these climate responses to those under nominal solar minimum conditions, we expose climate patterns that are hidden under the large climate variability in the latter.

1 Introduction

The Sun is the ultimate driver of the Earth atmosphere system, and it is of great interest to explore the impacts of solar variability on the atmosphere on time scales ranging from solar flares to multiple solar cycles (Gray et al., 2010). While the solar signal in the stratosphere and above is stronger with the large variability at ultraviolet (UV) and shorter wavelengths (Marsh et al., 2007), it is much weaker in the troposphere and at the Earth surface, with global mean surface temperature variation less than 0.1K (Gray et al., 2010), consistent with the $\lesssim$0.1% change of total solar irradiance (TSI) over a solar cycle. Regional climate, on the other hand, may respond more strongly (Meehl et al., 2009; Ineson et al., 2011; Gray et al., 2016), and feedback and amplification mechanisms have been postulated by examining reanalysis and climate model results (Haigh, 1996; Kodera & Kuroda, 2002; Kodera & Shibata, 2006; Matthes et al., 2006; Meehl et al., 2009; Chiodo et al., 2012; Théblemont et al., 2015). However, the robustness of the solar signal in regional climate is still being debated (Chiodo et al., 2019), and it is challenging to establish a clear pathway by which the solar variability can affect the regional climate, and to understand climate sensitivity to solar forcing. One modeling strategy to address the challenge is to increase the solar variability signal by hypothetically increasing the TSI or SSI variability in the climate models (Meehl et al., 2013; Maycock et al., 2015; Ineson et al., 2015), though the SSI changes employed may not be constrained by the underlying solar physics. Constraint has been suggested from reconstructions of historical solar irradiance (e.g. during Maunder Minimum). Although reconstruction methods suffer from large uncertainties (Shapiro et al., 2011; Schrijver et al., 2011), they can be used as scenarios for climate simulations to explore sensitivity to solar forcing. For example, Spiegl and Langematz (2020) applied grand solar minimum scenarios based on reconstruction by Shapiro et al. (2011) to a chemistry-climate model and identified regional climate responses.

In this study, we will address this challenge by adapting a solar forcing that would result from a solar photosphere without magnetic field, produced by a non-magnetic, hydrodynamic (HD) solar simulation. While such a scenario is not a likely representation of a grand solar minimum, it is the most extreme quiet Sun (EQS) scenario that is possible within the limits set by the physics of the solar photosphere. More extreme forcing would require deeper seated changes in the stellar structure of the Sun.

2 Methods

2.1 Numerical Simulation of Quiet Sun Scenarios and Irradiance

Rempel (2020) performed simulations of the quiet Sun, i.e. solar granulation with a mixed polarity small-scale magnetic field, in order to quantify the sensitivity of TSI and SSI to the strength of the quiet Sun magnetic field. In these models the mixed polarity magnetic field is maintained by a small-scale turbulent dynamo that was first studied in a solar-like setup by Vögler and Schüssler (2007) and later refined by Rempel (2014, 2018). In particular the latter demonstrated that the saturation field strength is dependent on the formulation of the bottom boundary that parametrizes the coupling of the photosphere to the deeper convection zone. Rempel (2020) took advantage of this boundary dependence in order to create quiet Sun models with varying field strengths. Of relevance to the current study are the non-magnetic, hydrodynamic (HD) reference and a current quiet sun reference (small-scale dynamo with ∼69G unsigned vertical flux density at optical depth of unity – denoted as SSD69). Rempel (2020) found a TSI sensitivity of about 0.14% per 10G of unsigned flux in the photosphere. This rather high TSI sensitivity implies that only a moderate change of the quiet Sun by 10% in field strength would cause a TSI variation comparable to the observed solar cycle TSI variability.

In addition to the TSI, Rempel (2020) also computed SSI in the 200 - 10,000 nm spectral range using Kurucz/Castelli Opacity Distribution Functions (ODFs) (see Rempel (2020) for further detail). We use from Rempel (2020) the models HD and SSD69 to derive the most extreme solar minimum forcing consistent with physics of the solar photosphere by computing the SSI change that is expected from removing all magnetic fields in the solar photosphere. We emphasize that this is not a likely scenario for a grand solar minimum, and serves in this study solely as an extreme forcing, which is still consistent with known solar physics principles, to investigate climate response and climate sensitivity that are easily obscured by the natural climate variability. Since Rempel (2020) computed SSI only for the range from 200-10,000 nm, between 121 nm (Lyman-alpha) and 200 nm the SSI is deduced from an empirical scaling relationship. SSI from SSD69 is similar to the SSI of modern solar minimum (Smin), though TSI from SSD69 is not exactly equal to the TSI of Smin that is adopted for Coupled Model Intercomparison Project Phase 5 (CMIP5) experiments (Kopp & Lean, 2011; Marsh et al., 2013). In order to make meaningful comparisons between the climate simulations, SSI values of HD and SSD69 are further scaled by multiplying a scaling factor, TSI(Smin)/TSI(SSD69). With this scaling, the corresponding TSI for HD is 1350.08 Wm^{-2}, 0.77% lower than the nominal solar minimum TSI value (also the scaled SSD69 value) (1360.43 Wm^{-2}). Detailed quantitative difference between SSI(HD) and SSI(SSD69) can be found in Rempel (2020).

2.2 CESM Whole Atmosphere Community Climate Model and Numerical Experiments

The Whole Atmosphere Community Climate Model (WACCM) is one of the atmosphere components of the NCAR Community Earth System Model version 1.1 (CESM 1.1) with its upper boundary extended to the lower thermosphere (∼140 km). The WACCM configuration used in this study is the same as that employed for the Chemistry-Climate Model Initiative (CCMI). As described in Morgenstern et al. (2017), this version of WACCM includes chemistry packages for the troposphere and stratosphere (Tilmes et al., 2016; Wegner et al., 2013) and for the mesosphere and lower thermosphere (Marsh et al., 2013). As described in Garcia et al. (2017), this version also includes a gravity wave parameterization scheme updated from the one used in earlier versions (Garcia et al., 2007), which leads to improved model climatology. The CESM/WACCM for this study includes the fully coupled Parallel Ocean Program (POP) ocean component (Danabasoglu et al., 2012). All WACCM simulations discussed in this study are with coupled ocean component. The horizontal resolution of WACCM for the simulation is $1.9° \times 2.5°$ in latitude and longitude, and there are 66 vertical levels. The horizontal resolution of POP is ∼1°.

CESM/WACCM simulations are first performed under nominal solar maximum (TSI: 1361.93 Wm^{-2}, referred as Smax run) and solar minimum (TSI: 1360.43 Wm^{-2}, Smin) conditions. Both sets of simulations are initialized by the same equilibrated pre-industrial control simulation, and the emission level is held constant during the 200-year simulation. Therefore the focus of this study is to examine responses to perpetual solar forcing change. The annually averaged global mean surface temperature from Smax and Smin simulations are shown in Fig. 1.

CESM/WACCM simulations are then performed using the SSI and TSI from the HD solar simulation, with the same initial condition as Smax and Smin, and the simulation length is 200 years. In order to further discern the effects by solar heating near the Earth surface and by the ozone heating in the stratosphere, two additional simulations have been performed: in HDVIR the SSI at wavelengths longer than 320 nm is taken from the HD SSI while at shorter wavelengths the SSI is the same as in Smin; in HDUV the SSI at wavelengths shorter than 320 nm is taken from HD SSI while at longer wavelengths the SSI the same as in Smin. The TSI for HDVIR and HDUV are 1350.84 $\mathrm{Wm^{-2}}$ and 1359.76 $\mathrm{Wm^{-2}}$, respectively. The initialization and length of the simulations are the same as HD.

A summary of the CESM/WACCM simulations with different solar forcing is presented in Table 1.

2.3 Significance Tests

WACCM is intrinsically chaotic, and any difference in the initial conditions and/or the model forcing (e.g. solar and geomagnetic forcing) would lead to divergence of the simulations (Liu et al., 2009). Therefore, the later 150 years of the solar minimum (HD, HDVIR, HDUV and Smin) and 200 years of the Smax simulations are used to provide large enough sample for significance tests.

In this analysis, statistical tests are conducted on the null hypothesis that quantities from the solar minimum simulations (HD, HDVIR, HDUV, and Smin) are the same as those of Smax. Two types of significance tests have been employed: gridpoint-by-gridpoint two-sided Student T-test, and the method to control false discovery rate (FDR) described in Ventura et al. (2004). The FDR approach can control the probability of falsely rejecting the null hypothesis for spatially correlated data to a pre-specified level (10% is used in this study). It is found that the two methods yield nearly identical test results for the large forcing cases (HD and HDVIR), and subtle differences for the weak forcing cases (HDUV and Smin), especially for latitude-height patterns of zonal mean quantities. Only test results from the FDR method are presented in the paper.

To further establish the robustness of the signal, significance tests have also been conducted for subsets of the solar minimum simulations by splitting the later 150 years into two 75-year groups. It is found that in all cases the results are very similar, though the magnitudes from the later 75 years are slightly larger. No results from these tests are shown in the paper, since no additional information is gained.

It is also noted that in our figures the stippling is applied to regions where the FDR is higher than 10% (thus the difference is not significant). This is to achieve a better visualization of the signal patterns that are statistically significant.

3 Results

CESM/WACCM simulations have been performed under EQS conditions, under nominal solar maximum and minimum conditions, as well as with only the visible and infrared (VIR) or ultraviolet (UV) part of the SSI changed to that from the EQS conditions. The annual averages of the global mean surface temperature (T_s) from the Smax, HD, HDVIR, and HDUV simulations are shown in Fig. 2(a), with T_s of HD, HDVIR, and HDUV lower than Smax by 0.833, 0.79, and 0.149 K, respectively, more than the cooling of Smin (0.087 K) (all averages over the last 150 years of the simulations). T_s in all these cases show significant multi-decadal variability, though the magnitudes of the cooling in HD and HDVIR are much larger than the magnitude of the variability.

We first examine the sensitivity of the model climate system to the solar forcing changes, by following Gregory et al. (2004); Bacmeister et al. (2020) and calculating the global feedback parameter. This is to linearly regress the radiative imbalance to the changes of global averaged surface temperature : $\lambda = \delta\overline{T_s}/\delta\overline{R_N}$, where $R_N = R_S - R_L$, with R_S and R_L being the downward shortwave and upward longwave radiative fluxes, respectively. As noted by Gregory et al. (2004), this method does not require a steady state to be reached, and simulations for all 200 years are used in our calculation. From Table 1, it is seen that $\lambda(HD)$ and $\lambda(HDVIR)$ are 1.64±0.17 and 1.62±0.17 Wm^{-2}K^{-1} respectively. With initial $R_N(HD)$ and $R_N(HDVIR)$ being 2.15 and 2.5 Wm^{-2}K^{-1} respectively, and considering the standard deviation of R_N to be 0.48 Wm^{-2}K^{-1}, the ΔT_s intercepts are found to be -1.31±0.46 K and -1.54±0.49 K for HD and HDVIR respectively. For HDUV and Smin, the global feedback parameters are slightly larger, with larger uncertainties. The ΔT_s intercepts are found to be -0.56±0.38 K and -0.71±0.42 K. The average cooling over the last 150 years of the respective simulations are less than these intercept values. The differences probably suggest that the simulations have not reached equilibrium state yet. The linear assumption and large variabilities (especially for HDUV and Smin) may also contribute to the difference. On the other hand, the global mean surface temperature changes for each unit of TSI changes in the cases of HD, HDVIR and HDUV are all around 0.07 K/Wm^{-2}, slightly larger than that from the Smin simulation (0.0578 K/Wm^{-2}). This is comparable to the values reported in previous studies (White et al., 1997; Gray et al., 2010).

The time scales of initial T_s adjustment differ in the northern hemisphere (NH, 30-90°N), southern hemisphere (SH, 30-90°S) and at low latitudes: several years in NH and about 3 decades in SH and at low latitudes (Fig. 2 (b-d)). It is also noted that T_s still trends down afterward, but at a much slower rate. This is most evident in the global mean and SH mean values. Such differences in the adjustment time scales should be taken into consideration for proper lead/lag regression analysis for solar cycle signals. This slow trend is likely related to the ocean model equilibration, which requires millennial time scale simulations, though significant adjustments are usually complete within the first few centuries. 200-year long simulations are too short for the Atlantic meridional overturning circulation (AMOC) to reach a true equilibrium state, and there are likely additional changes in SSTs associated with convective activities. However, these usually impact small spatial scale deep water formation regions. This study focuses on climate and air-sea interactions on larger scales, and the "quasi-equilibrium" climatologies from the last 150 years of the 200-year HD, HDVIR, HDUV, and Smin simulations are compared with the Smax simulations.

3.1 Surface temperature patterns in response to solar forcing changes

Global patterns of T_s differences between HD/HDVIR and Smax for northern and southern winter seasons (DJF and JJA respectively) show significant cooling throughout most of the globe (Fig. 2(e and i), (f and j)), with the most pronounced cooling found in the Arctic (-2K), over Eurasia and North America (-1 to -2K) (especially their northeast coastal regions, up to -4K), and the Antarctic (-1K) (especially its coastal region in the south Indian Ocean sector, -3K) during their respective winter seasons. In particular, sea ice growth is noted in the western Bering Sea and the Southern Ocean with the strongest cooling. The coastal cooling coincides generally with regions with the largest upward sensible heat flux (da Silva et al., 1995), suggesting strong heat loss to the air blowing from the continents, which are colder due to the reduced solar activity. The strong atmosphere cooling over the Arctic also leads to the thickening of sea-ice. This is probably associated with the Arctic amplification, where the sea-ice change plays an important role (Screen & Simmonds, 2010). The strong Arctic cooling results in brine rejection in the ocean, making the Arctic saltier and denser. The dense water finds its way into the deep northern North Atlantic around 1000-m depth, and pushes the North Atlantic Deep Water (NADW) cell deeper without much change in the upper ocean or northward heat transport, as can be seen from Fig. 3. The AMOC from the Smax simulation is provided as a reference in the Supporting Information (Figure S1).

At lower latitudes, the cooling over continents is generally more pronounced than over the ocean for both seasons. A notable exception is the significant cooling (-1K) over the tropical central eastern Pacific, and this is in contrast to the previous report of tropical eastern Pacific cooling during peak solar years (Meehl et al., 2009), but is consistent with the analysis and simulation results by Misios et al. (2019); Spiegl and Langematz (2020). In contrast to the overall cooling, there is a distinct warm anomaly in the central North Atlantic region in HD and HDVIR (up to ∼0.5 K during DJF). A similar warm anomaly is seen in Spiegl and Langematz (2020) (the strong grand solar minimum scenario simulation in that study).

Similar spatial patterns are noted in the surface temperature changes in HDUV (Fig. 2(g and k)), albeit with smaller magnitude in comparison with HD and HDVIR. Coolings of 0.6–0.8 K and ∼0.4 K over NH continents and equatorial central eastern Pacific are one half and one third, respectively, of those in HDVIR. A prominent warm anomaly is found during JJA extending from Weddell Sea to Ross Sea. While there is no net warming at that location in HD/HDVIR, probably because it is offset by the strong surface cooling, a similar zonal wavenumber 1 structure is noted. The similarities between the HDUV and HDVIR underscore responses that are enhanced by the solar forcing changes in the stratosphere and in the troposphere/surface. Similar patterns are also seen in the surface temperature difference between Smin and Smax (e.g. cooling of 0.4–0.5K over NH continents and 0.3K over central eastern Pacific).

While Fig. 2(e-l) show the patterns of surface temperature change with respect to the solar maximum reference, it is also helpful to examine the surface temperature changes of HDVIR and HDUV with respect to Smin. Since the UV (VIR) part of the SSI in the former (latter) case is identical to that in Smin, the comparison would elucidate surface responses to changes in VIR (UV) alone. From Fig. 4 it is seen that surface temperature responses to VIR changes are very similar to those seen in Fig. 2(e-f) and (i-j), in terms of their spatial patterns, amplitudes and significance level. On the other hand, the temperature responses to UV changes are weaker. They are also weaker than those seen

Fig. 2(g-k). Spatial patterns of regional temperature change are similar in many places, though with smaller magnitude–thus smaller signal to noise ratio and lower significance level. For example, during DJF at 45°N the average cooling over Eurasia (0–135°) drops from 1.08K (VIR) to 0.29K (UV), and the warming over the North Atlantic (20–45°W) drops from 0.34K to 0.06K; at the equator the average cooling over central/eastern Pacific drops from 0.76K to 0.12K. During JJA, the cooling over the eastern part of Antarctic (0–90° at 80°S) decreases from 1.1K (VIR) to 0.22K (UV). There are also several regions where the responses are notably different: regions in North America poleward of 45°N during DJF and over Southern Ocean during JJA. Over the Weddell Sea at 80°S a cooling of 0.49K (VIR) changes to warming of 0.49K (UV). It is quite remarkable that the responses in HD are linearly additive of the VIR and UV responses in most of these regions, even though the latter may not appear to be statistically significant. Furthermore, it is seen that the regional surface temperature responses to UV change is 15–30% of those to VIR change at places where the responses are similar. For comparison, the global mean surface temperature difference between UV and Smin (0.06K, Table 1) is 8.6% of the difference between VIR and Smin (0.7K).

3.2 Regional changes of tropospheric winds and air-sea interaction

Surface and regional climate changes are closely associated with tropospheric winds, which are found to respond significantly to solar forcing changes (Fig. 5). At 300 hPa, the meridional wind changes (± 2 ms^{-1}) during boreal winter display a robust pattern in the NH that is remarkably similar (with opposite signs) to the intermediate scale stationary wave changes in response to a warming climate (Simpson et al., 2016; Wills et al., 2019). This reflects perturbations to the circumglobal teleconnection pattern and is caused mainly by the weakening of the eastward subtropical upper tropospheric wind (by about 2 ms^{-1} below tropopause between 20–40°N, Fig. 7) (Branstator, 2002; Simpson et al., 2016), which alters the dominant length scale of stationary waves that are supported by the subtropical wave guide. The slower zonal wind also leads to the decreases of the propagation speed of the PWs, and is likely responsible for the equatorward shift of large-scale PWs. Similar stationary wave patterns–most prominently the wind perturbations extending from Southwest North America (southward phase), Mexico (northward phase), Gulf of Mexico (southward phase), and north Brazil/Atlantic Ocean (northward phase)–are seen in all four solar minimum simulations (Supporting Information Figure S2(i-p)). By comparing the Smin and HD results, therefore, we can identify regional climate responses that may not appear statistically significant in the former. For example, regional cooling by equatorward winds over Europe, Middle East, East Asia, western North America, southern Africa, and South America are likely robust features during solar minimum (Fig. 2(h and l), Supporting Information Figure S2(l and p)).

In addition to the regional changes over major continents, northward/eastward wind anomaly is seen over the North Atlantic at both 300 hPa and 850 hPa, most significant during boreal winter (Fig. 5). This change enhances the north-eastward ocean circulation, thus causes the prominent warming of the central North Atlantic Ocean as seen in surface temperature (Fig. 2). It is also seen that the trade wind over equatorial Pacific (from $\sim$150°E to the west coast of South America) is enhanced (2 ms^{-1}). Along with the enhancement of eastward wind at 300 hPa, it suggests an enhancement of the Walker circulation, leading to cooling over the tropical eastern Pacific (Fig. 2). This is a robust feature seen in all cases–with a cooling of 1K (HD and HDUV) and 0.2K (HDUV and Smin) extending from 170°E to the west coast of South America during DJF–again suggesting a stronger response from the superposition of similar troposphere/surface and stratospheric responses. This change is consistent with the recent finding of a slower Walker circulation at solar maximum (Misios et al., 2019). It also contrasts the finding by Meehl et al. (2009), which might result from a sampling issue (Misios et al., 2019).

During austral winter (and spring), the strongest zonal wind deceleration can extend down to the surface at mid to high latitudes (Fig. 6). At 54°S this is most significant around 0° and 45°W in HD and HDUV respectively. Changes with similar longitude-height structures are found in all four solar minimum cases, with varying levels of significance. The westward wind anomaly near the surface induces a poleward Ekman transport and thus a warm anomaly around Weddell Sea. This is most evident in HDUV case, both because of the significant westward wind change and the lack of strong surface cooling (Figs. 2 (k) and 4(d)).

3.3 Troposphere and stratosphere coupling and its hemispheric differences

As already alluded to above, the tropospheric changes are caused by atmosphere circulation changes in the troposphere and above in response to solar forcing changes.

From Fig. 7(a and c) (and Supporting Information Figure S3 a and c), it is seen that the subtropical zonal wind in the upper troposphere and stratosphere (most prominently in the winter hemisphere) weakens due to the reduction of diabatic heating during both DJF and JJA. Wind changes with similar magnitudes (1.5–2ms^{-1}) occur in HDVIR (Supporting Information Figure S3 e and g). Weakening of the subtropical wind (up to 30° latitude in the winter hemisphere, due to the poleward shift of the wind system) at the upper troposphere is seen in HDUV and Smin (Supporting Information Figure S3 i/k and m/o), though the changes are weaker ($\sim$0.5 ms^{-1}) and not statistically significant. These are consistent with the weaker changes of intermediate scale stationary waves seen in HDUV and Smin (Figure S2).

The winter (and also spring time) stratospheric wind changes at mid to high latitudes differ significantly between the two hemispheres, with a weak increase (not statistically significant) in the NH and a significant decrease (up to -4 ms^{-1}) in the SH. The former is in apparent contrast to the dynamical responses expected for solar minimum conditions when stratospheric differential heating is reduced and zonal forcing by planetary wave (PW) increases (Kodera & Kuroda, 2002). Further examination of monthly differences shows that the weakening of winter stratospheric wind and its poleward and downward shift from early to late winter, as expected from Kodera and Kuroda (2002) and Ineson et al. (2011), are seen in HDUV in both hemispheres and in HD and HDVIR only in the SH (Supporting Information Figure S4), suggesting differences in PW responses to solar forcing changes in the troposphere and in the stratosphere. Hemispheric difference is also seen in the thermal response to solar forcing (From Fig. 7(b and d)). Apart from the general cooling in these simulations expected from reduced solar forcing, there is a warming in the lower stratosphere and upper troposphere in the SH winter that becomes statistically significant around the tropopause, with a peak of 0.3K. On the other hand, no significant warming is seen in the NH winter.

These hemispheric differences stem from different PW responses in the two hemispheres (Fig. 7(e-h)). The vertical component of Eliassen-Palm flux (EP$_z$) shifts equatorward in the troposphere and decreases in the stratosphere (albeit not statistically significant due to the large wave variability during boreal winter) in the NH, and correspondingly the westward forcing by the PWs weakens in the stratosphere. The SH changes are the opposite, with both EP$_z$ and wave forcing increasing significantly. This is also seen from the longitudinal and height structures of the meridional wind and temperature (Supporting Information Figure S5), with the wind and temperature changes becoming increasingly out of phase with the climatological zonal wavenumber 1 perturbations in the NH above 30hPa, while increasingly in phase in the SH. It is found that PW with zonal wavenumber 1 accounts for most of the hemispheric differences at mid to high latitudes (Fig. 8 and Supporting Information Figure S2 (a-h)): it decreases during DJF in NH and increases during JJA and even more significantly in SON in SH in the troposphere and stratosphere.

The decrease during boreal winter is consistent with wave 1 increase during a warming climate, which is found to be affected by the subtropical wind and zonally asymmetric diabatic heating changes (Wang & Kushner, 2011). On the other hand, this decrease is likely offset by the weakening of winter stratospheric wind at mid-high latitudes, which tends to increase EP_z of wave 1 (Kodera & Kuroda, 2002). Since the subtropical wind changes are similar between the two hemispheres, the wave 1 increase in SH should result mostly from changes of tropospheric wave sources, and the superposition leads to significant weakening of the winter stratospheric wind. There has not been previous studies specifically on the change of wave 1 in SH, but it is evidenced in Joseph et al. (2004). That study suggested that the forcing from transients tends to enhance (weaken) wave 1 at high northern (southern) latitudes during winter in a warming climate (thus the opposite in a cooling scenario). In contrast to wave 1, PWs with wavenumber 2–4 and 6 increase during both hemispheric winters, and the increase of wave 2-3 extends into the stratosphere.

Differences in responses to tropospheric/surface forcing change and to stratospheric forcing change can be further elucidated by comparing HD, HDVIR, and HDUV with Smin simulations for all four seasons (Fig. 9). For DJF, the NH EP_z responses to tropospheric/surface forcing (HDVIR) and stratospheric forcing (HDUV) are the opposite in the middle/upper stratosphere and high latitudes, with a decrease in the former and increase in the latter. The response in HD is weaker and is a superposition of the two: a decrease in the upper stratosphere and increase lower down. None of these changes are statistically significant. No remarkable changes are seen in either hemisphere during MAM. During JJA, the SH EP_z increase becomes quite large throughout the stratosphere at higher latitudes, though still not statistically significant. However, it shows a small increase in HDVIR and a small decrease in HDUV, which are apparently not linearly additive in comparison to the changes of HD. This is likely due to small signal to noise ratio during JJA in these cases. On the other hand, large (∼20%) and statistically significant changes are seen in HD during SON throughout the southern stratosphere at mid to high latitudes. Correspondingly, rather large (though not statistically significant) EP_z increases are seen in both HDVIR and HDUV (∼5% and 10%, respectively). Furthermore, the EP_z increases in HD are larger than the sum of EP_z changes in HDVIR and HDUV for both JJA and SON. This suggests that a positive feedback between the tropospheric and stratospheric responses to the solar forcing changes.

These comparisons show that EP_z responses in the stratosphere to tropospheric/surface forcing change are opposite for hemispheric winters (extending into spring time for SH): decrease in NH and increase in the SH. On the other hand, the responses to stratospheric forcing change are similar: increase in both hemispheres at higher latitudes. This response to stratospheric forcing change is consistent with the postulation by Kodera and Kuroda (2002). Therefore, the tropospheric/surface forcing and stratospheric forcing are offsetting during boreal winter and becomes stronger during austral winter and spring. Similar changes are seen when comparing HD and Smax (Figs. 7 (e and g)), and HDVIR, HDUV, and Smin with Smax (Supporting Information Figure S6) with different levels of statistical significance. The seasonal/hemispheric variation is also consistent with that seen in wave 1 amplitude changes (Fig. 8).

The PW differences lead to differences in the interplay between dynamical and radiative forcing during hemispheric winters. The decrease of PW forcing in the NH leads to stronger stratospheric winter jet, weaker Brewer-Dobson (BD) circulation, and less adiabatic warming (cooling) in the polar (equatorial) tropopause/stratosphere. The dynamical and radiative effects thus offset each other in the boreal winter stratosphere for zonal wind change, but lead to stronger cooling, as reflected in the magnitude and significance levels of the change. This is exactly the opposite during austral winter, with stronger dynamical/radiative effects in decelerating the zonal wind but offsetting in thermal forcing. These processes and the hemispheric differences are summarized in Table 2.

4 Summary and Conclusion

While the EQS simulations show stronger climate responses than Smin, they still display remarkable general similarities, including the surface temperature, zonal mean states, wave fluxes and structures, and regional climate. Such similarities under different solar minimum conditions highlight the robust responses of the climate system to solar forcing change. Robustness of the responses is further established by applying rigorous significance test in our analysis.

Solar radiative heating changes in the troposphere and stratosphere both lead to subtropical wind changes that alter the intermediate scale stationary waves and regional climate in the troposphere in a similar way. The patterns of these changes are also similar to those found in a warming climate, but with opposite signs. Control simulations by only altering part of SSI discern the responses to changes in troposphere/surface forcing and to stratospheric forcing: solar VIR minimum causes PW wave 1 decrease in boreal winter and wave 1 increase in austral winter, while UV minimum tends to increase PW 1 at high latitudes in the stratosphere during both winters. The magnitude of the former change is larger than the latter, and is responsible for the hemispheric differences of the climate responses.

The responses may not appear significant based on statistical sampling when the solar forcing change is nominal, but those in EQS simulations are significant and unambiguous. This study suggests the possibility of checking the physical significance of the former by comparing to the latter. Therefore, climate simulations under EQS conditions provides a means in exposing the patterns hidden under the large climate variability. Furthermore, comparisons of HD, HDVIR and HDUV simulations shed light on the underlying mechanisms and elucidate processes where the solar forcing changes in troposphere/surface and stratosphere are similar or different. With cooling in both troposphere and middle atmosphere, the EQS simulations also provide a forcing scenario that contrasts with a warming climate, (warming in the troposphere and cooling above).

Figure 1: Annually averaged global mean surface temperature from simulations under nominal solar maximum (Smax, black line) and solar minimum (Smin, orange line) conditions.

Figure 2: Annually averaged mean surface temperature over (a) the whole globe, (b) northern hemisphere (30°N to the North Pole), (c) tropical region (30°S to 30°N), (d) southern hemisphere (30°S to the South Pole) from Smax (black), HD (blue), HDVIR (orange), and HDUV (red) simulations. Average surface temperature differences (color contours) between years 50-200 of HD, HDVIR, HDUV, and Smin and Smax simulations for DJF (e–h, respectively) and JJA (i–l, respectively). Contour lines are mean temperature from Smax simulations. Unstippled regions are differences that are statistically significant at the 95% level from Student t-test. The white scale in (e-h) corresponds to the averages of the global mean surface temperature change for these cases: cooling by 0.833, 0.79, 0.149, and 0.087K in HD, HDVIR, HDUV, and Smin respectively in comparison with Smax.

Figure 3: Differences of (a) salinity (unit: practical salinity unit, psu) and (b) Atlantic meridional overturning circulation (AMOC) (unit: Sv.) between years 50 to 200 of HD simulations and Smax simulations.

Figure 4: (a-b) Similar to Fig. 2 f and g, but with respect to Smin. (c-d) Similar to Fig. 2 j and k.

Figure 5: Differences of average (a) meridional wind and (b) zonal wind between 50–200 year of HD and Smax simulations at 300 hPa for boreal winter (DJF). Line contours are average winds (in a, solid: northward (a) and eastward (b), contour intervals: $2ms^{-1}$ (a) and $2ms^{-1}$ (b)) from Smax simulations. (c-d): Similar to (a-b), but for 850 hPa.

Figure 6: Differences of average zonal wind (color contours) between 50–200 year of (a) HD, (b) HDVIR, (c) HDUV and (d) Smin and Smax simulations at 54°S for austral winter (JJA). Line contours are average zonal wind from Smax simulations (solid: eastward, contour intervals: $5\mathrm{ms}^{-1}$).

Figure 7: Differences of average zonal mean zonal wind (color contours) between 50–200 year of HD and Smax simulations for (a) DJF and (c) JJA. Line contours are average zonal mean zonal wind from Smax simulations (contour intervals: 15 ms^{-1}). (b) and (d): similar to (a) and (c) but for average zonal mean temperature differences (color contour and grey line contours for differences less than 1K, with 0.25 K intervals). Line contours are average zonal mean temperature from Smax simulations (contour intervals: 10 K). (e) and (g): similar to (a) and (c) but for average vertical EP flux component differences. The EP flux (unit: Pa m) is normalized by $p^{0.75}$ (p: atmosphere pressure) to better visualize the change at all altitudes (color contour). Line contours are average normalized vertical EP flux component from Smax simulations (contour intervals: 10×10^2). (f) and (h): similar to (a) and (c) but for average EP flux divergence differences (color contour). Line contours are average EP flux divergence from Smax simulations (contour intervals: 1 $\mathrm{ms}^{-1}\mathrm{d}^{-1}$).

Figure 8: Differences of zonal wavenumber 1 amplitude of geopotential height between 50–200 year of HD and Smax simulations for (a) DJF, (b) MAM, (c) JJA and (d) SON (color contour). Line contours are average wave 1 amplitude from Smax simulations (contour intervals: 50 m).

Figure 9: Upper panel: Differences of average vertical EP flux component between 50–200 year of HD and Smin simulations for DJF, MAM, JJA and SON. Middle panel: Similar to upper panel, but for HDVIR and Smin. Lower panel: Similar to upper panel, but for HDUV and Smin. The EP flux (unit: Pa m) is normalized by $p^{0.75}$ (p: atmosphere pressure) to better visualize the change at all altitudes (color contour). Line contours are average normalized vertical EP flux component from Smin simulations (contour intervals: 10×10^2).

Table 1: CESM/WACCM simulations and the solar forcing used, the corresponding total solar irradiance (TSI), the global mean surface temperature (T_s) averaged over the whole simulation period (Smax) and the last 150 years of the simulations (HD, HDVIR, HDUV, and Smin), and the global feedback parameter based on all 200 years of simulations.

Table 2: Summary of the changes of stationary planetary wave 1 (PW1), mean temperature (T), and mean zonal wind (U) in the winter stratosphere of the northern and southern hemispheres (NH/SH) due to changes of direct radiative forcing and dynamical forcing. BD refers to Brewer-Dobson circulation, which is primarily driven by the planetary wave and causes adiabatic warming in the winter stratosphere.

Open Research

CESM is a community model and is available for download (`https://www.cesm.ucar.edu/models/cesm1.1/index.html`). CESM model outputs are served through the Climate Data Gateway (`https://www.earthsystemgrid.org/`).

Acknowledgments

The CESM project is primarily supported by the National Science Foundation (NSF). This material is based on work supported by the National Center for Atmospheric Research (NCAR), which is a major facility sponsored by the NSF under Cooperative Agreement 1852977. Efforts by HLL, MR, SCS and JMM are partially supported by NASA grant NNX16AB82G. High-performance computing support by the NASA Advanced Supercomputing (NAS) Division at Ames Research Center provided by NASA High-End Computing (HEC) Program is acknowledged. We thank I. Simpson for valuable comments, and D. Bailey and A. Altuntas for their help with the sea-ice and ocean model analysis, respectively.

References

Bacmeister, J. T., Hannay, C., Medeiros, B., Gettelman, A., Neale, R., Fredriksen, H. B., ... Otto-Bliesner, B. (2020). Co2 increase experiments using the cesm: Relationship to climate sensitivity and comparison of cesm1 to cesm2. *Journal of Advances in Modeling Earth Systems*, *12*. doi: 10.1029/2020MS002120

Branstator, G. (2002). Circumglobal teleconnections, the jet stream waveguide, and the north atlantic oscillation. *Journal of Climate*, *15*, 1893-1910.

Chiodo, G., Calvo, N., Marsh, D. R., & Garcia-Herrera, R. (2012). The 11 year solar cycle signal in transient simulations from the whole atmosphere community climate model. *Journal of Geophysical Research: Atmospheres*, *117*. doi: 10.1029/2011JD016393

Chiodo, G., Oehrlein, J., Polvani, L. M., Fyfe, J. C., & Smith, A. K. (2019). Insignificant influence of the 11-year solar cycle on the north atlantic oscillation. *Nature Geoscience*, *12*, 94-99. doi: 10.1038/s41561-018-0293-3

da Silva, A., Young, C., & Levitus, S. (1995). *Atlas of surface marine data 1994. Vol.1: Algorithms and procedures* (NOAA Atlas NESDIS No. 6). Washington DC: U.S. Dept. of Commerce, NOAA.

Danabasoglu, G., Bates, S. C., Briegleb, B. P., Jayne, S. R., Jochum, M., Large, W. G., ... Yeager, S. G. (2012). The ccsm4 ocean component. *Journal of Climate*, *25*, 1361-1389. doi: 10.1175/JCLI-D-11-00091.1

Garcia, R. R., Marsh, D. R., Kinnison, D. E., Boville, B. A., & Sassi, F. (2007). Simulation of secular trends in the middle atmosphere, 1950-2003. *J. Geophys. Res.*, *112*. doi: 10.1029/2006JD007485

Garcia, R. R., Smith, A. K., Kinnison, D. E., Álvaro de la Cámara, & Murphy, D. J. (2017). Modification of the gravity wave parameterization in the whole atmosphere community climate model: Motivation and results. *Journal of the Atmospheric Sciences*, *74*, 275-291. doi: 10.1175/JAS-D-16-0104.1

Gray, L. J., Beer, J., Geller, M., Haigh, J. D., Lockwood, M., Matthes, K., ... White, W. (2010). Solar influences on climate. *Reviews of Geophysics*, *48*. doi: 10.1029/2009RG000282

Gray, L. J., Woollings, T. J., Andrews, M., & Knight, J. (2016). Eleven-year solar cycle signal in the nao and atlantic/european blocking. *Quarterly Journal of the Royal Meteorological Society*, *142*, 1890-1903. doi: 10.1002/qj.2782

Gregory, J. M., Ingram, W. J., Palmer, M. A., Jones, G. S., Stott, P. A., Thorpe, R. B., ... Williams, K. D. (2004). A new method for diagnosing radiative forcing and climate sensitivity. *Geophysical Research Letters*, *31*. doi: 10.1029/2003GL018747

Haigh, J. D. (1996). The impact of solar variability on climate. *Science*, *272*, 981-984. doi: 10.1126/science.272.5264.981

Ineson, S., Maycock, A. C., Gray, L. J., Scaife, A. A., Dunstone, N. J., Harder, J. W., ... Wood, R. A. (2015). Regional climate impacts of a possible future grand solar minimum. *Nature Communications*, *6*, 7535. doi: 10.1038/ncomms8535

Ineson, S., Scaife, A. A., Knight, J. R., Manners, J. C., Dunstone, N. J., Gray, L. J., & Haigh, J. D. (2011). Solar forcing of winter climate variability in the northern hemisphere. *Nature Geoscience*, *4*, 753-757. doi: 10.1038/ngeo1282

Joseph, R., Ting, M., & Kushner, P. J. (2004). The global stationary wave response to climate change in a coupled gcm. *J. Climate*, *17*, 540-556.

Kodera, K., & Kuroda, Y. (2002). Dynamical response to the solar cycle. *Journal of Geophysical Research: Atmospheres*, *107*. doi: 10.1029/2002JD002224

Kodera, K., & Shibata, K. (2006). Solar influence on the tropical stratosphere and troposphere in the northern summer. *Geophysical Research Letters*, *33*. doi: 10.1029/2006GL026659

Kopp, G., & Lean, J. L. (2011). A new, lower value of total solar irradiance: Evidence and climate significance. *Geophysical Research Letters*, *38*(1). doi: https://doi.org/10.1029/2010GL045777

Liu, H.-L., Sassi, F., & Garcia, R. R. (2009). Error growth in a whole atmosphere climate model. *Journal of the Atmospheric Sciences*, *66*, 173-186.

Marsh, D. R., Garcia, R., Kinnison, D., Boville, B., Sassi, F., & Solomon, S. (2007). Modeling the whole atmosphere response to solar cycle changes in radiative and geomagnetic forcing. *Journal of Geophysical Research*, *112*. doi: 10.1029/2006JD008306

Marsh, D. R., Mills, M. J., Kinnison, D. E., Lamarque, J.-F., Calvo, N., & Polvani, L. M. (2013). Climate Change from 1850 to 2005 Simulated in CESM1(WACCM). *Journal of Climate*, *26*, 7372–7391. doi: 10.1175/JCLI-D-12-00558.1

Matthes, K., Kuroda, Y., Kodera, K., & Langematz, U. (2006). Transfer of the solar signal from the stratosphere to the troposphere: Northern winter. *Journal of Geophysical Research: Atmospheres*, *111*. doi: 10.1029/2005JD006283

Maycock, A. C., Ineson, S., Gray, L. J., Scaife, A. A., Anstey, J. A., Lockwood, M., … Osprey, S. M. (2015). Possible impacts of a future grand solar minimum on climate: Stratospheric and global circulation changes. *Journal of Geophysical Research: Atmospheres*, *120*, 9043-9058. doi: 10.1002/2014JD022022

Meehl, G. A., Arblaster, J. M., & Marsh, D. R. (2013). Could a future "Grand Solar Minimum" like the maunder minimum stop global warming? *Geophysical Research Letters*, *40*, 1789-1793. doi: 10.1002/grl.50361

Meehl, G. A., Arblaster, J. M., Matthes, K., Sassi, F., & van Loon, H. (2009). Amplifying the pacific climate system response to a small 11-year solar cycle forcing. *Science*, *325*, 1114–1118. doi: 10.1126/science.1172872

Misios, S., Gray, L. J., Knudsen, M. F., Karoff, C., Schmidt, H., & Haigh, J. D. (2019). Slowdown of the walker circulation at solar cycle maximum. *Proceedings of the National Academy of Sciences*, *116*, 7186–7191. doi: 10.1073/pnas.1815060116

Morgenstern, O., Hegglin, M. I., Rozanov, E., O'Connor, F. M., Abraham, N. L., Akiyoshi, H., ... Zeng, G. (2017). Review of the global models used within phase 1 of the chemistry–climate model initiative (ccmi). *Geoscientific Model Development*, *10*, 639–671. doi: 10.5194/gmd-10-639-2017

Rempel, M. (2014, July). Numerical Simulations of Quiet Sun Magnetism: On the Contribution from a Small-scale Dynamo. *Astrophysics Journal*, *789*, 132. doi: 10.1088/0004-637X/789/2/132

Rempel, M. (2018, June). Small-scale Dynamo Simulations: Magnetic Field Amplification in Exploding Granules and the Role of Deep and Shallow Recirculation. *Astrophysics Journal*, *859*, 161. doi: 10.3847/1538-4357/aabba0

Rempel, M. (2020). On the contribution of quiet Sun magnetism to solar irradiance variations: Constraints on quiet Sun variability and grand minimum scenarios. *Astrophysical Journal*, *894*. doi: 10.3847/1538-4357/ab8633

Schrijver, C. J., Livingston, W. C., Woods, T. N., & Mewaldt, R. A. (2011). The minimal solar activity in 2008–2009 and its implications for long-term climate modeling. *Geophysical Research Letters*, *38*. doi: 10.1029/2011GL046658

Screen, J. A., & Simmonds, I. (2010). The central role of diminishing sea ice in recent arctic temperature amplification. *Nature*, *464*, 1334-1337. doi: 10.1038/nature09051

Shapiro, A. I., Schmutz, W., Rozanov, E., Schoell, M., Haberreiter, M., Shapiro, A. V., & Nyeki, S. (2011). A new approach to the long-term reconstruction of the solar irradiance leads to large historical solar forcing. *Astrophysics Journal*, *529*, A67. doi: 10.1051/0004-6361/201016173

Simpson, I. R., Seager, R., Ting, M., & Shaw, T. A. (2016). Causes of change in northern hemisphere winter meridional winds and regional hydroclimate. *Nature Climate Change*, *6*, 65–70. doi: 10.1038/nclimate2783

Spiegl, T., & Langematz, U. (2020). Twenty-first-century climate change hot spots in the light of a weakening sun. *Journal of Climate*, *33*(9), 3431 - 3447. Retrieved from `https://journals.ametsoc.org/view/journals/clim/33/9/jcli-d-19-0059.1.xml` doi: 10.1175/JCLI-D-19-0059.1

Théblemont, R., Matthes, K., Omrani, N.-E., Kodera, K., & Hansen, F. (2015). Solar forcing synchronizes decadal north atlantic climate variability. *Nature Communications*, *6*, 8268. doi: 10.1038/ncomms9268

Tilmes, S., Lamarque, J.-F., Emmons, L. K., Kinnison, D. E., Marsh, D., Garcia, R. R., ... Blake, N. (2016). Representation of the community earth system model (cesm1) cam4-chem within the chemistry-climate model initiative (ccmi). *Geoscientific Model Development*, *9*, 1853–1890. doi: 10.5194/gmd-9-1853-2016

Ventura, V., Paciorek, C. J., & Risbey, J. S. (2004). Controlling the proportion of falsely rejected hypotheses when conducting multiple tests with climatological data. *Journal of Climate*, *17*(22), 4343 - 4356. doi: 10.1175/3199.1

Vögler, A., & Schüssler, M. (2007, April). A solar surface dynamo. *Astronomy and Astrophysics*, *465*, L43-L46. doi: 10.1051/0004-6361:20077253

Wang, L., & Kushner, P. J. (2011). Diagnosing the stratosphere-troposphere stationary wave response to climate change in a general circulation model. *Journal of Geophysical Research: Atmospheres*, *116*. doi: https://doi.org/10.1029/2010JD015473

Wegner, T., Kinnison, D. E., Garcia, R. R., & Solomon, S. (2013). Simulation of polar stratospheric clouds in the specified dynamics version of the whole atmosphere community climate model. *Journal of Geophysical Research: Atmospheres*, *118*, 4991-5002. doi: 10.1002/jgrd.50415

White, W. B., Lean, J., Cayan, D. R., & Dettinger, M. D. (1997). Response of global upper ocean temperature to changing solar irradiance. *Journal of Geophysical Research: Oceans*, *102*, 3255-3266. doi: https://doi.org/10.1029/96JC03549

Wills, R. C. J., White, R. H., & Levine, X. J. (2019). Northern hemisphere stationary waves in a changing climate. *Current Climate Change Reports*, *5*, 372–389. doi: 10.1007/s40641-019-00147-6

Figure 1.

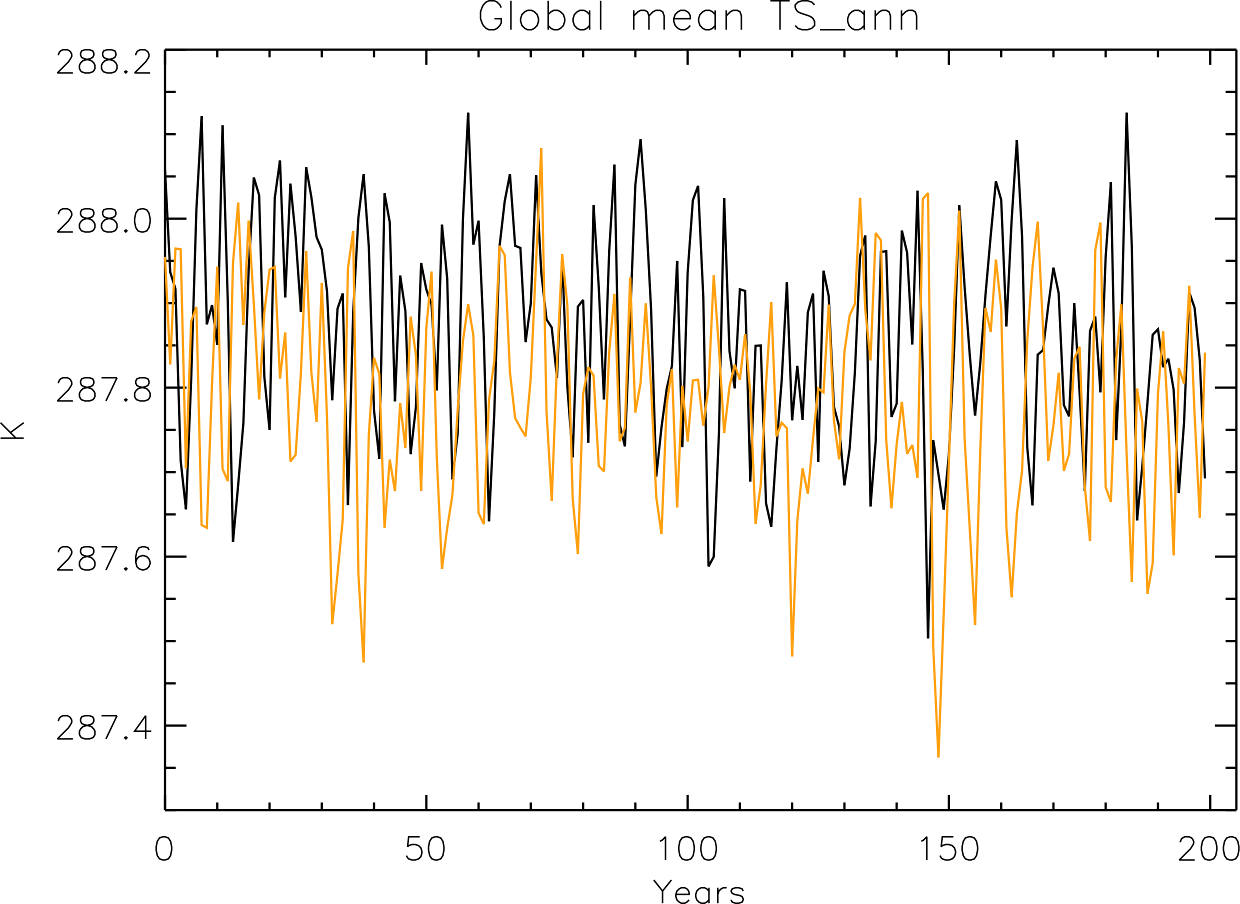
Global mean TS_ann
288.2
288.0
287.8
287.6
287.4
K
0
50
100
150
200
Years

Figure 2.

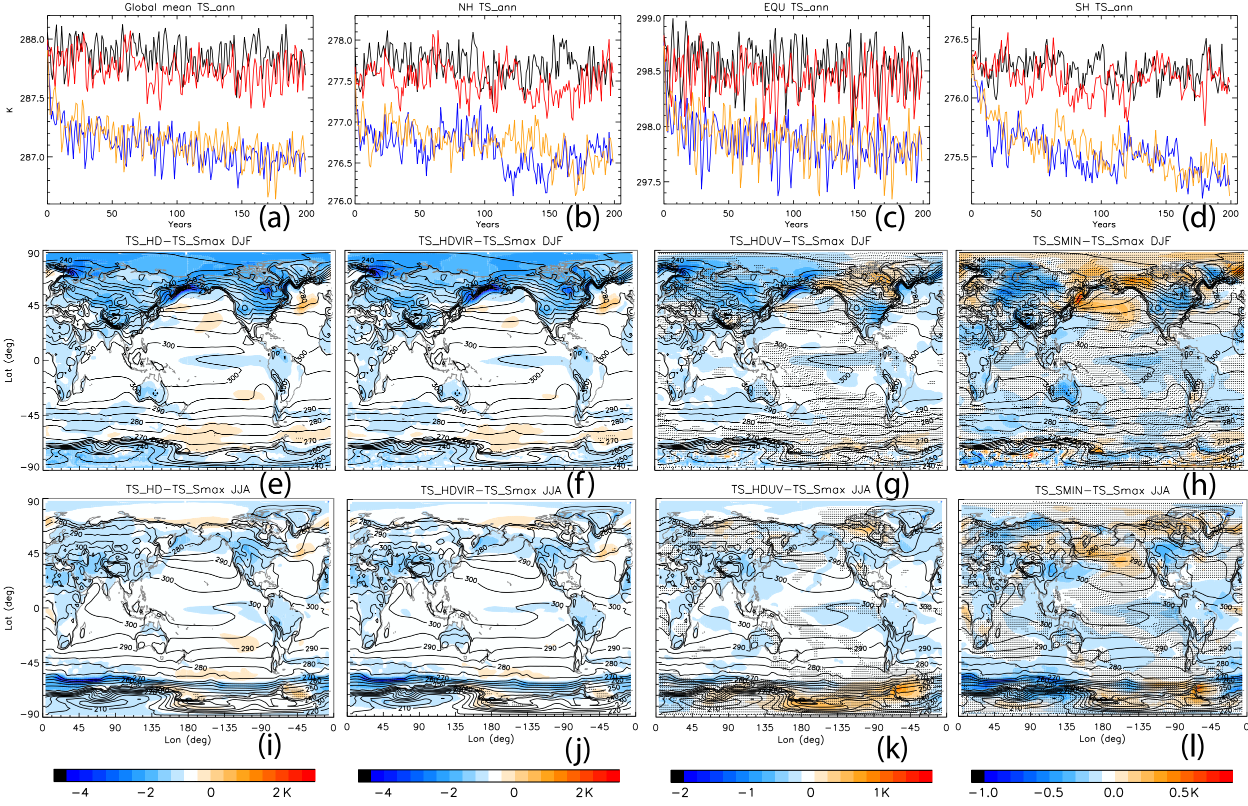

Global mean TS_ann
NH TS_ann
EQU TS_ann
SH TS_ann
K
Years
(a)
(b)
(c)
(d)
TS_HD−TS_Smax DJF
TS_HDVIR−TS_Smax DJF
TS_HDUV−TS_Smax DJF
TS_SMIN−TS_Smax DJF
(e)
(f)
(g)
(h)
TS_HD−TS_Smax JJA
TS_HDVIR−TS_Smax JJA
TS_HDUV−TS_Smax JJA
TS_SMIN−TS_Smax JJA
Lat (deg)
Lon (deg)
(i)
(j)
(k)
(l)
−4 −2 0 2 K
−4 −2 0 2 K
−2 −1 0 1 K
−1.0 −0.5 0.0 0.5 K

Figure 3.

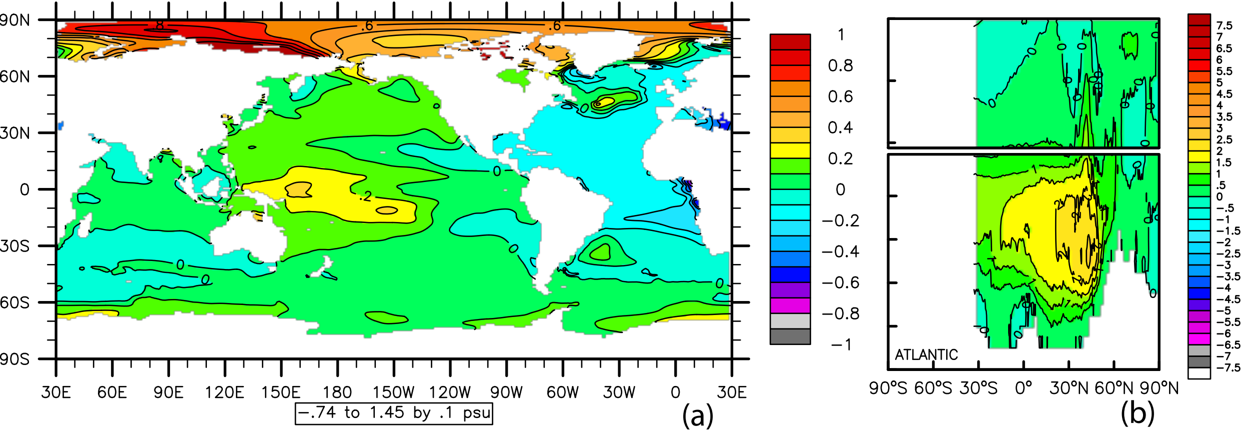

90N
60N
30N
0
30S
60S
90S
30E 60E 90E 120E 150E 180 150W 120W 90W 60W 30W 0 30E
−.74 to 1.45 by .1 psu
(a)
1
0.8
0.6
0.4
0.2
0
−0.2
−0.4
−0.6
−0.8
−1
ATLANTIC
90°S 60°S 30°S 0° 30°N 60°N 90°N
(b)
7.5
7
6.5
6
5.5
5
4.5
4
3.5
3
2.5
2
1.5
1
.5
0
−.5
−1
−1.5
−2
−2.5
−3
−3.5
−4
−4.5
−5
−5.5
−6
−6.5
−7
−7.5

Figure 4.

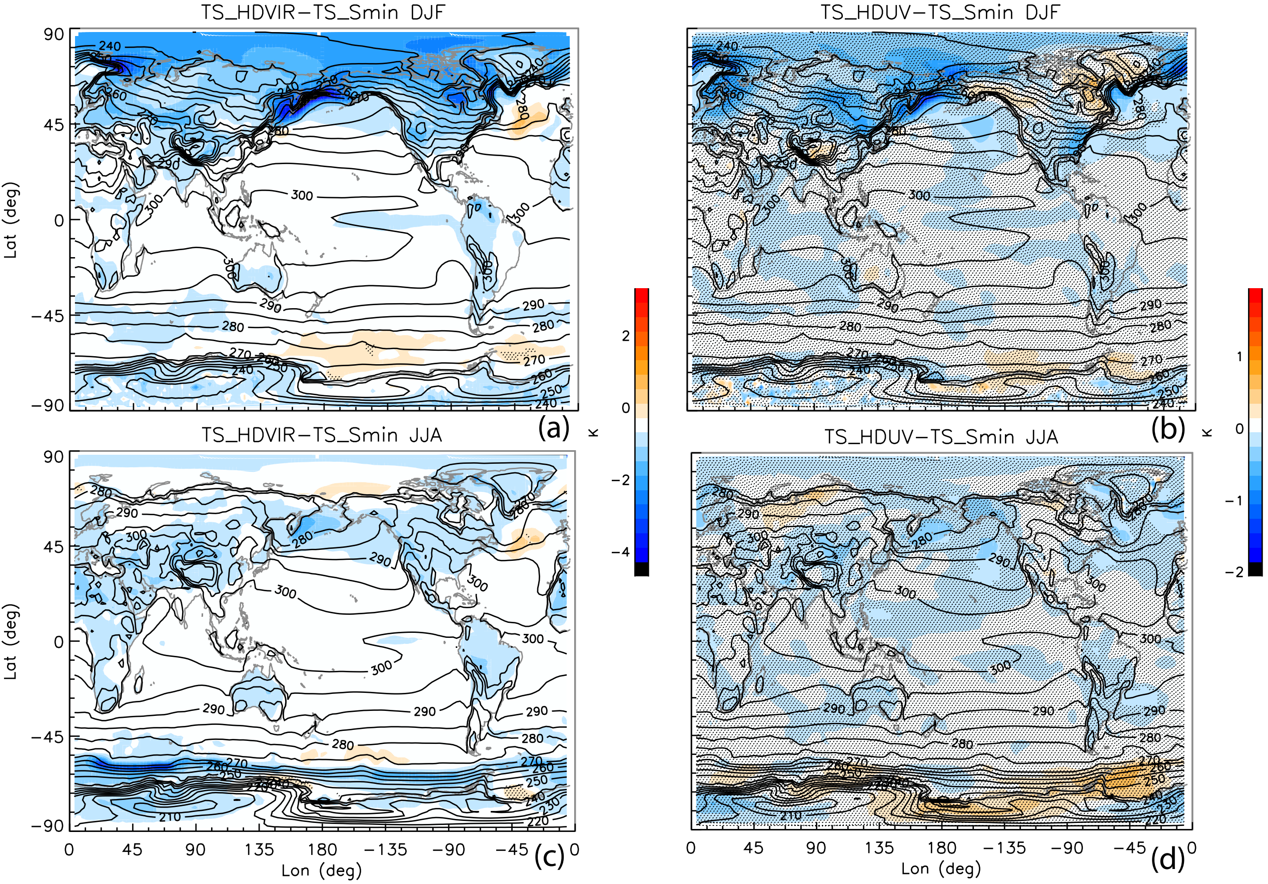

TS_HDVIR−TS_Smin DJF
TS_HDUV−TS_Smin DJF
TS_HDVIR−TS_Smin JJA
TS_HDUV−TS_Smin JJA
Lat (deg)
Lon (deg)
K
(a)
(b)
(c)
(d)

Figure 5.

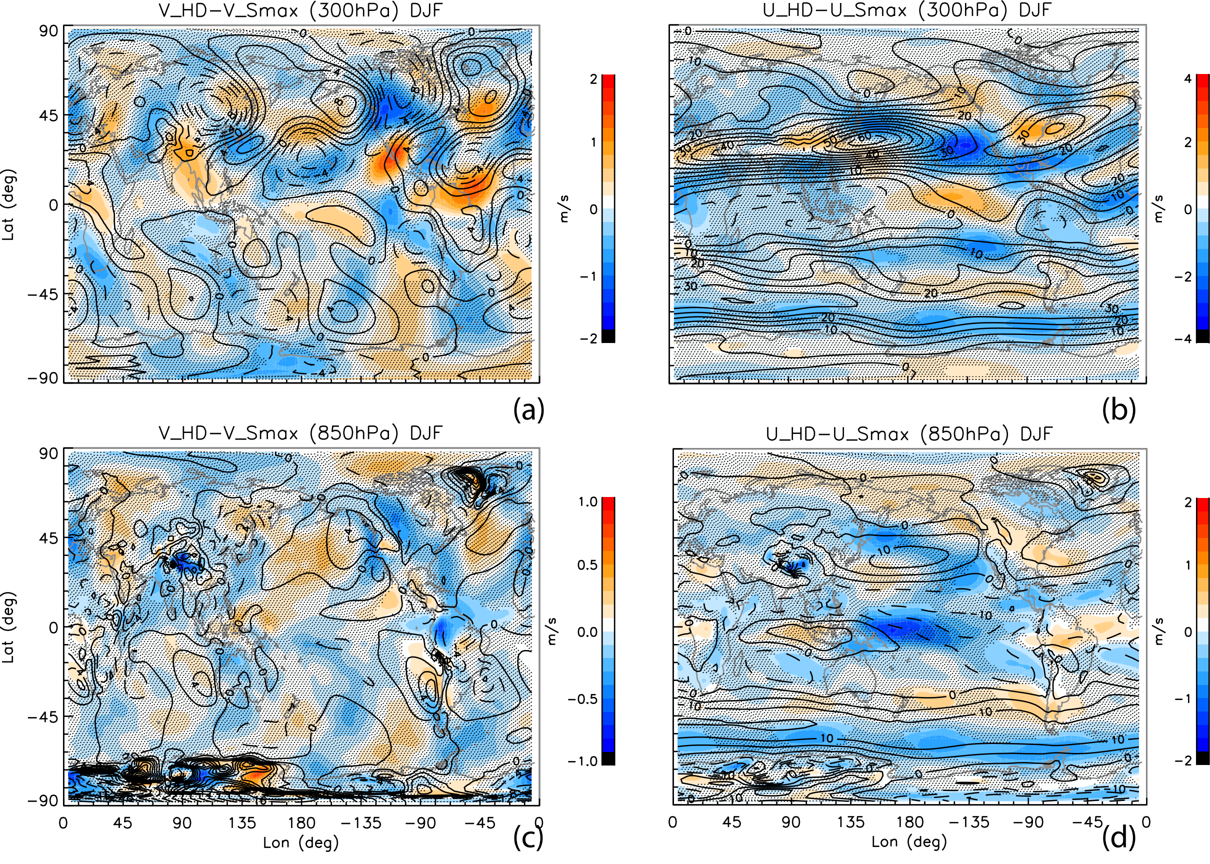

V_HD−V_Smax (300hPa) DJF
U_HD−U_Smax (300hPa) DJF
V_HD−V_Smax (850hPa) DJF
U_HD−U_Smax (850hPa) DJF
Lat (deg)
Lon (deg)
m/s
90
45
0
−45
−90
0
45
90
135
180
−135
−90
−45
0
2
1
0
−1
−2
4
2
0
−2
−4
1.0
0.5
0.0
−0.5
−1.0
2
1
0
−1
−2
(a)
(b)
(c)
(d)

Figure 6.

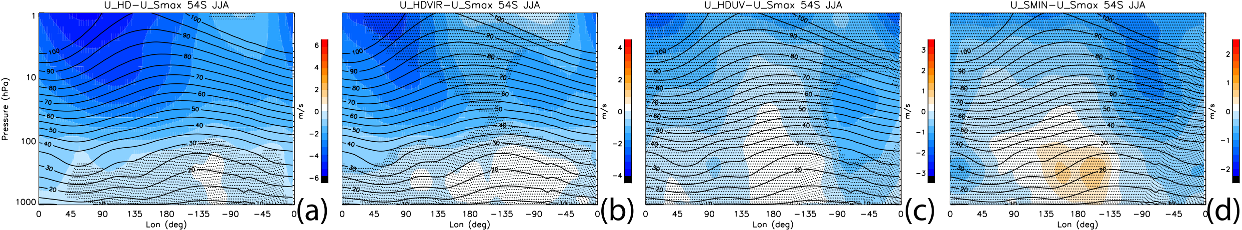
U_HD−U_Smax 54S JJA
U_HDVIR−U_Smax 54S JJA
U_HDUV−U_Smax 54S JJA
U_SMIN−U_Smax 54S JJA
Pressure (hPa)
Lon (deg)
m/s
(a)
(b)
(c)
(d)

Figure 7.

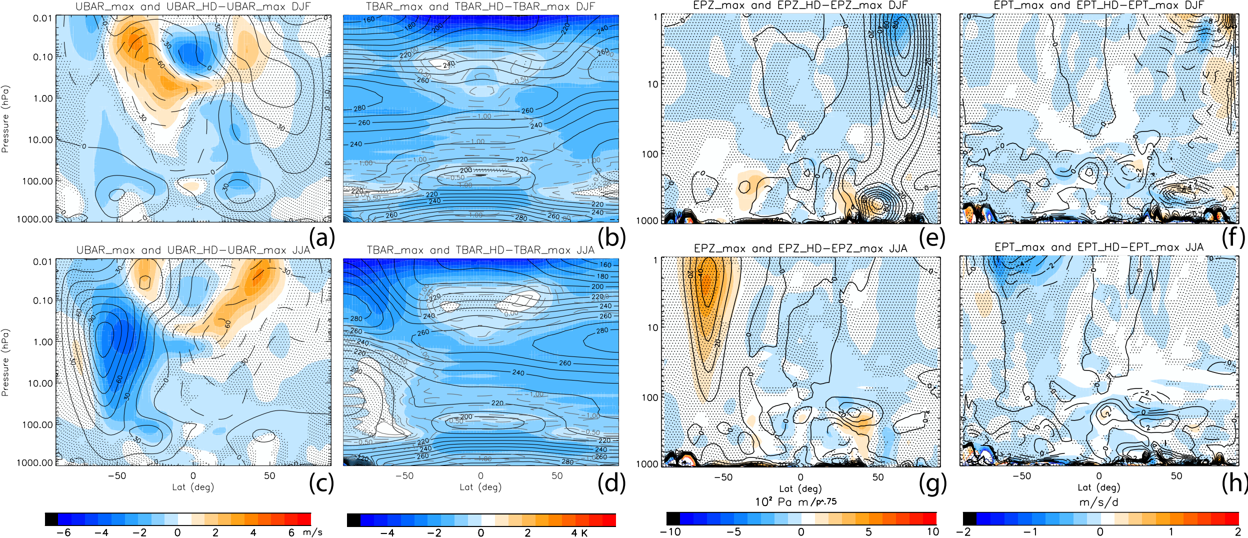
UBAR_max and UBAR_HD−UBAR_max DJF
TBAR_max and TBAR_HD−TBAR_max DJF
EPZ_max and EPZ_HD−EPZ_max DJF
EPT_max and EPT_HD−EPT_max DJF
UBAR_max and UBAR_HD−UBAR_max JJA
TBAR_max and TBAR_HD−TBAR_max JJA
EPZ_max and EPZ_HD−EPZ_max JJA
EPT_max and EPT_HD−EPT_max JJA
(a)
(b)
(c)
(d)
(e)
(f)
(g)
(h)
Pressure (hPa)
Lat (deg)
m/s
K
10² Pa m/p^.75
m/s/d

Figure 8.

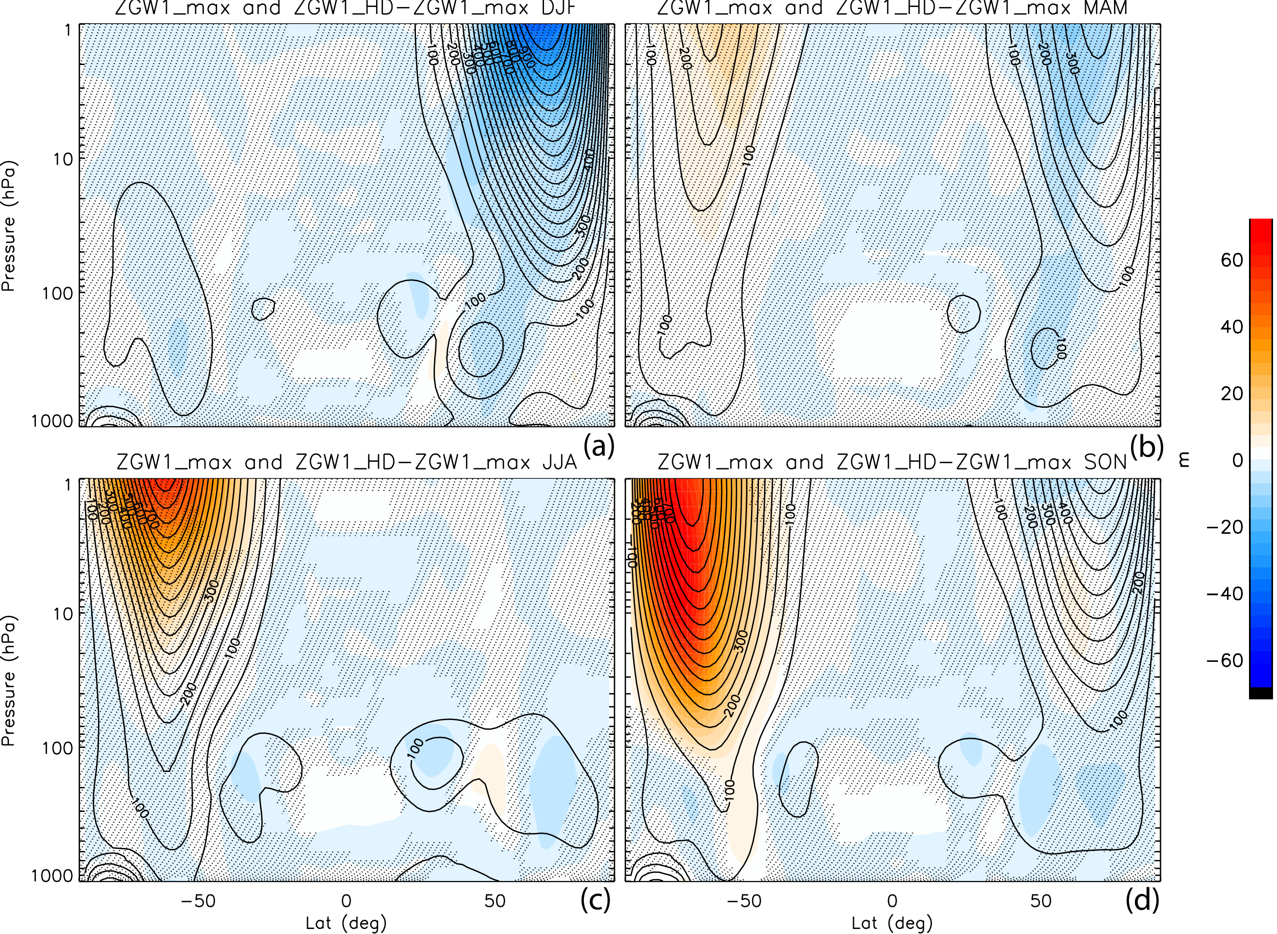

ZGW1_max and ZGW1_HD−ZGW1_max DJF
ZGW1_max and ZGW1_HD−ZGW1_max MAM
ZGW1_max and ZGW1_HD−ZGW1_max JJA
ZGW1_max and ZGW1_HD−ZGW1_max SON
Pressure (hPa)
Lat (deg)
(a)
(b)
(c)
(d)
m
60
40
20
0
−20
−40
−60

Figure 9.

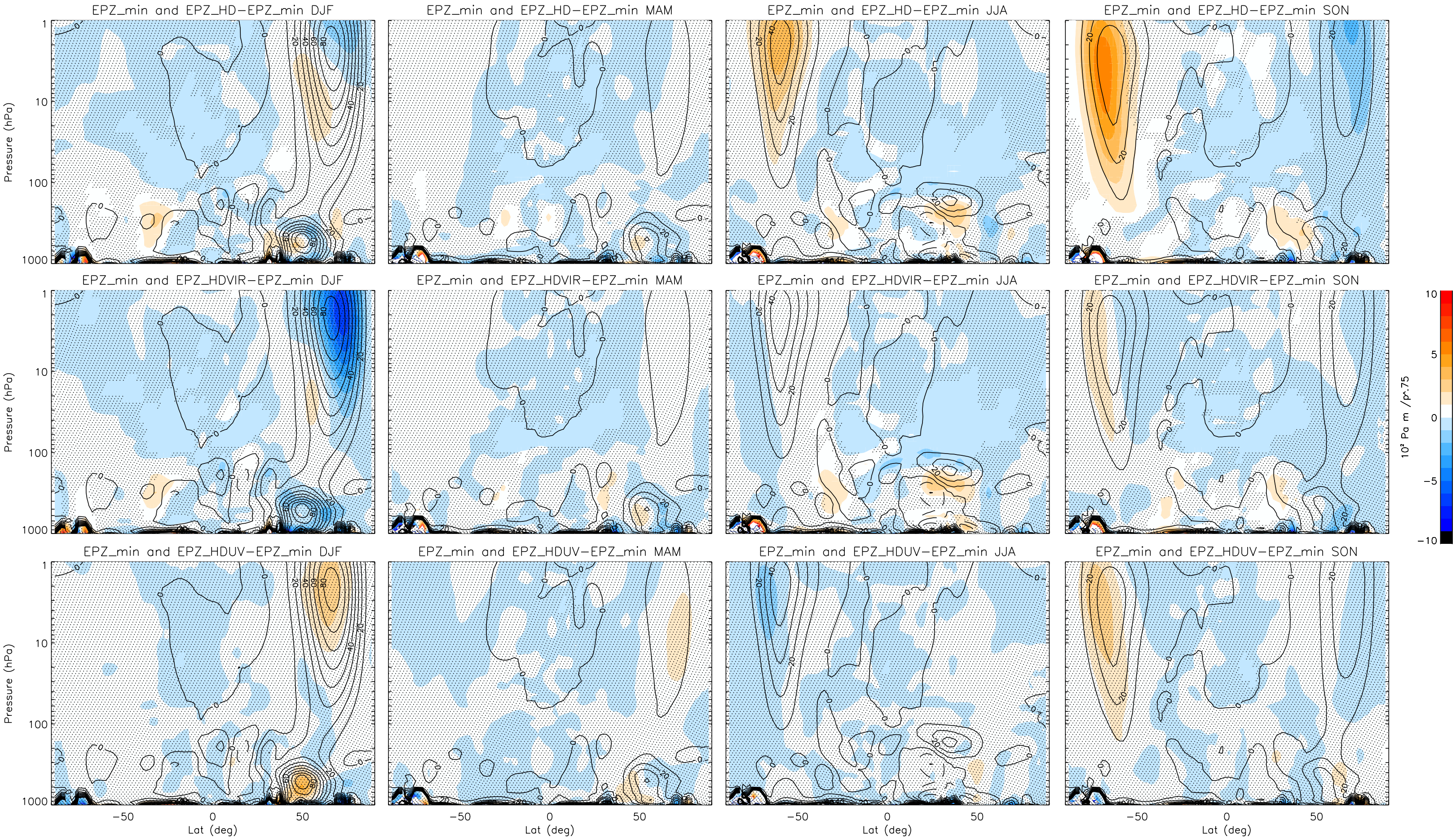

EPZ_min and EPZ_HD-EPZ_min DJF
EPZ_min and EPZ_HD-EPZ_min MAM
EPZ_min and EPZ_HD-EPZ_min JJA
EPZ_min and EPZ_HD-EPZ_min SON
EPZ_min and EPZ_HDVIR-EPZ_min DJF
EPZ_min and EPZ_HDVIR-EPZ_min MAM
EPZ_min and EPZ_HDVIR-EPZ_min JJA
EPZ_min and EPZ_HDVIR-EPZ_min SON
EPZ_min and EPZ_HDUV-EPZ_min DJF
EPZ_min and EPZ_HDUV-EPZ_min MAM
EPZ_min and EPZ_HDUV-EPZ_min JJA
EPZ_min and EPZ_HDUV-EPZ_min SON
Pressure (hPa)
Lat (deg)
10² Pa m /p^.75

Solar Forcing Used for Driving CESM/ WACCM Simulations	Nominal solar maximum (Smax)	Nominal solar minimum (Smin)	Non-magnetic, hydrodynamic (HD) reference	SSI(Smin) ($\lambda \leq 320$nm)+ SSI(HD) ($\lambda > 320$nm) (HDVIR)	SSI(HD) ($\lambda \leq 320$nm)+ SSI(Smin) ($\lambda > 320$nm) (HDUV)
TSI (Wm^{-2})	1361.93	1360.43	1350.08	1350.84	1359.76
Ts (K)	287.87	287.78	287.04	287.08	287.72
Global feedback parameter ($Wm^{-2}K^{-1}$)		1.68 (0.22)	1.64 (0.17)	1.62 (0.17)	1.75 (0.22)

	PW1(NH)	T(NH)	U(NH)	PW1(SH)	T(SH)	U(NH)
Radiative		Cooling	Slower		Cooling	Slower
Dynamical	Weaker/ Weaker BD	Cooling	Faster	Stronger/ Stronger BD	Warming	Slower
Net		Strong Cooling	Variable		Variable	Much Slower